International Journal of Hydrogen Energy 173 (2025) 151390

Contents lists available at ScienceDirect

International Journal of Hydrogen Energy

journal homepage: www.elsevier.com/locate/he

Structural tailoring of metal-coordinated salen-tetraphenylethene-based conjugated microporous polymers for superior active alkaline oxygen evolution electrocatalysis

Yang-Chin Kao [a,1], Tapomay Mondal [a,1], Wei-Hsuan Chang [a], Mohamed Gamal Mohamed [a,b,*], Shiao-Wei Kuo [a,c,**]

[a] Department of Materials and Optoelectronic Science, Center for Functional Polymers and Supramolecular Materials, National Sun Yat-Sen University, Kaohsiung, 804, Taiwan
[b] Department of Chemistry, Faculty of Science, Assiut University, Assiut, 71515, Egypt
[c] Department of Medicinal and Applied Chemistry, Kaohsiung Medical University, Kaohsiung, 807, Taiwan

ARTICLE INFO

Keywords:
Tetraphenylethene
Salen
Conjugated microporous polymers
Sonogashira coupling
Oxygen evolution reaction

ABSTRACT

The development of earth-abundant, metal-organic electrocatalysts for the oxygen evolution reaction (OER) is crucial for sustainable hydrogen production. Herein, we report a series of conjugated microporous polymers (CMPs) derived from 1,1,2,2-tetrakis(4-ethynylphenyl) ethane (TPE-T) and phenylenebis(azaneylylidene))bis (methaneylylidene))bis(3-bromophenol) [OPDI-2Br] using a simple and efficient Sonogashira alkyne coupling reaction, either non-coordinated and pre-coordinated with ferrous (Fe^{2+}), cobalt(II) (Co^{2+}), and nickel(II) (Ni^{2+}) ions. N_2 adsorption–desorption analyses demonstrate that metal coordination induces torsional strain in the OPDI backbone, disrupting π–π stacking, generating nonplanar architectures, and producing hierarchical micro/mesoporosity. Electrochemical evaluation in aqueous potassium hydroxide (KOH, 1.0 M) shows that the Co-coordinated CMP (TPE-OPDI-Co) achieves a low overpotential of 400 mV at 10 mA cm^{-2}, a Tafel slope of 74 mV dec^{-1}, and a charge-transfer resistance of79.4 Ω. Its electrochemical surface area (4.47 cm^2) and long-term durability (Δ $E < 7$ mV after 1000 cycles) rival those of benchmark Ruthenium(IV) oxide (RuO_2) and Iridium(IV) oxide (IrO_2)/C catalysts. This work highlights metal coordination as a versatile strategy for tailoring the porosity and electronic structure of CMPs to achieve high-performance OER electrocatalysis.

1. Introduction

The rapid depletion of fossil fuels and the escalating energy demands of modern society necessitate the development of sustainable and renewable energy sources [1–3]. In this context, electrochemical water splitting, which involves the hydrogen evolution reaction (HER) and the OER, has emerged as a promising route for the production of clean hydrogen [4–7]. Despite its potential, the overall efficiency of water splitting is significantly hindered by the sluggish kinetics of the OER, a process that involves a complex four-electron transfer mechanism [8–16]. Traditionally, precious metal-based catalysts, such as RuO_2 and IrO_2, have been regarded as benchmark electrocatalysts for the oxygen evolution reaction (OER) due to their exceptional activity. However, their scarcity and high cost severely restrict their large-scale application, prompting researchers to seek earth-abundant alternatives [17–30]. First-row transition metals such as Fe, Co, and Ni are desirable for this study due to their natural abundance, low cost, and demonstrated catalytic activity in alkaline media. Their multiple accessible oxidation states and favorable coordination chemistry enable the formation of stable complexes with organic ligands while maintaining structural integrity under electrochemical conditions [30,31]. In addition, these metals are highly compatible with conjugated polymer frameworks,

* Corresponding author. Department of Materials and Optoelectronic Science, Center for Functional Polymers and Supramolecular Materials, National Sun Yat-Sen University, Kaohsiung, 804, Taiwan.
** Corresponding author. Department of Materials and Optoelectronic Science, Center for Functional Polymers and Supramolecular Materials, National Sun Yat-Sen University, Kaohsiung, 804, Taiwan.
E-mail addresses: mgamal.eldin12@yahoo.com, mgaml.eldin12@aun.edu.eg (M.G. Mohamed), kuosw@faculty.nsysu.edu.tw (S.-W. Kuo).
[1] These authors contributed equally to this work.

https://doi.org/10.1016/j.ijhydene.2025.151390
Received 15 June 2025; Received in revised form 19 August 2025; Accepted 4 September 2025
Available online 8 September 2025

allowing for uniform dispersion of active sites and efficient electronic communication throughout the porous network. Collectively, these properties make Fe, Co, and Ni ideal candidates for designing robust, efficient, and scalable oxygen evolution catalysts based on organic–inorganic hybrid materials.

Porous organic polymers (POPs) have recently garnered attention due to their tunable porosity, high surface area, and versatile chemical functionality [31–38]. Among the different classes of POPs, including metal-organic frameworks (MOFs) [39], covalent organic frameworks (COFs) [40–42], and conjugated microporous polymers (CMPs) [43–45],CMPs are particularly attractive since they offer superior hydrothermal stability and can be synthesized via robust covalent bonding strategies [46–56]. Unlike MOFs and COFs, CMPs can easily incorporate functional building blocks, which is crucial for designing materials with enhanced catalytic performance [57–61]. The integration of the transition of metal species into a conjugated organic framework is an effective strategy to improve catalytic activity. The incorporation not only facilitates efficient charge transfer but also provides abundant active sites for the catalytic reaction [62–66]. This approach is especially promising for the development of advanced OER electrocatalysts.

Building upon this platform, transition metal complexes incorporating salen ligands have attracted considerable interest due to their strong chelating ability and exceptional capacity to stabilize metal ions. The tetradentate nature of salen ligands, featuring two nitrogen and two oxygen donor atoms, enables the formation of highly stable coordination complexes with a wide range of transition metals. These complexes exhibit well-defined geometries and electronic properties, making them valuable in various fields, including catalysis and coordination chemistry [20,67]. Salen-type metal complexes have demonstrated excellent redox and electrochemical properties, making them appealing candidates for various electrocatalytic applications [20,67]. Although these complexes have been extensively studied in the context of organic transformations [68,69], their potential in OER catalysis remains underexplored. By grafting transition metals such as Fe, Co, and Ni onto TPE-OPDI-based CMPs, one can harness the benefits of both the intrinsic catalytic activity of the metal centers and the robust, highly conjugated porous structure of CMPs [70]. Recent studies have shown that metal-modified porous frameworks, including metal-grafted COFs and MOFs, exhibit promising catalytic activity for water splitting. However, these materials often suffer from low hydrothermal stability and synthetic challenges that limit their practical applications. In contrast, CMPs offer a robust platform with high thermal and chemical stability, making them ideal for long-term electrocatalytic applications [71]. Furthermore, hybrid materials, such as metal-doped carbon nanostructures including graphene and carbon nanotubes (CNTs), have been investigated to further enhance catalytic efficiency [72].

We prepared a series of OPDI-2Br Schiff-base monomers bearing salen moieties in four variants, non-coordinated, Fe^{2+}-, Co^{2+}-, and Ni^{2+}-coordinated (OPDI-*M*-2Br), and then subjected each to Sonogashira coupling with TPE-T. This strategy yielded four CMPs, TPE-OPDI, TPE-OPDI-Fe, TPE-OPDI-Co, and TPE-OPDI-Ni, collectively referred to as the TPE-based CMP series. Covalent integration of the OPDI units produced highly conjugated, amorphous networks with accessible metal coordination sites, as supported by evidence from various analytical approaches. Nitrogen sorption analysis revealed that metal coordination induces backbone torsion and generating hierarchical micro/mesoporosity with Brunauer–Emmett–Teller surface areas rising from 4 m^2 g^{-1} (TPE-OPDI CMP) to 60, 154, and 281 m^2 g^{-1} for the TPE-OPDI-Fe, TPE-OPDI-Co, and TPE-OPDI-Ni CMPs, respectively. Electrochemical testing in 1.0 M KOH demonstrated that all three TPE-OPDI-M CMPs dramatically outperform the metal-free polymer in the oxygen evolution reaction (OER): TPE-OPDI-Co CMP achieves the lowest overpotential of 400 mV at 10 mA cm^{-2}, a Tafel slope of 74 mV dec^{-1}, a high electrochemical surface area (4.47 cm^2), and a minimal overpotential increase (<7 mV) after 1000 cycles, rivaling benchmark RuO_2. These results clearly illustrate that pre-metalation of the OPDI building blocks is a powerful strategy to tune CMP porosity, electronic structure, and catalytic accessibility, yielding highly active and durable OER electrocatalysts.

2. Experimental section

2.1. Materials

1,2-Diaminobenzene (98 %), cobalt(II) acetate anhydrous [Co$(CH_3COO)_2$, 98 %], nickel(II) acetate tetrahydrate [Ni$(CH_3COO)_2{\cdot}4H_2O$, 99 %], triphenylphosphine (PPh_3, 99 %), and ethanol (99.5 %) were purchased from Alfa Aesar. Pd$(PPh_3)_4$ (99 %) was obtained from Leyan, while N,N-dimethylformamide (DMF, 99.9 %) was sourced from DUKSAN. 4-Bromo-2-hydroxybenzaldehyde (99.5 %) and copper(I) iodide (CuI, 98 %) were acquired from Sigma-Aldrich. Iron(II) acetate anhydrous [Fe$(CH_3COO)_2$, 98 %] was supplied by Combi-Block. Hexane (95 %), N, N-diethylethanamine (Et_3N), and tetrahydrofuran (THF, 99.9 %) were obtained from Merck. Additionally, in our previous study [73–76], the synthesis of 1,1,2,2-tetrakis(4-ethynylphenyl)ethene (TPE-T) was successfully achieved and characterized.

2.2. Synthesis of OPDI-2Br

In a 100 mL round-bottom flask, 0.50 g (4.63 mmol) of 1,2-diaminobenzene, 1.86 g (9.25 mmol) of 4-bromo-2-hydroxybenzaldehyde, and 50 mL of ethanol were combined. The mixture was refluxed for 24 h and then allowed to cool to room temperature. The light-yellow product was obtained via filtration and treated with ethanol to remove residual monomers [Yield: 70 %] [Scheme S1].

2.3. Synthesis of OPDI-M-2Br

OPDI-2Br (0.45 g, 0.95 mmol) was individually combined with either Fe$(CH_3COO)_2$ (0.33 g, 1.89 mmol), Co$(CH_3COO)_2$ (0.336 g, 1.89 mmol), or Ni$(CH_3COO)_2{\cdot}4H_2O$ (0.47 g, 1.88 mmol) in 80 mL of THF using a 150 mL flask. The mixtures were stirred at 70 °C for 24 h at 600 rpm. After cooling to room temperature, 500 mL of hexane was added to induce precipitation, and the solid products were collected by filtration and further purified by washing the obtained solid by hot methanol. The isolated products were obtained as follows: OPDI-Fe-2Br as an orange solid (yield: 36 %), OPDI-Co-2Br as a brown solid (yield: 40 %), and OPDI-Ni-2Br as a red solid (yield: 58 %) [Scheme S2].

2.4. Synthesis of TPE-OPDI and TPE-OPDI-M CMPs

In separate reactions, OPDI-2Br (0.332 g, 0.70 mmol), OPDI-Co-2Br (0.415 g, 0.70 mmol), OPDI-Fe-2Br (0.41 g, 0.70 mmol), or OPDI-Ni-2Br (0.414 g, 0.70 mmol) was combined with TPE-T (0.15 g, 0.35 mmol), CuI (0.035 mmol), PPh_3 (0.034 mmol), and Pd$(PPh_3)_4$ (0.035 mmol) in a mixed solvent of DMF (18 mL) and Et_3N (18 mL). The reaction mixtures were refluxed at 90 °C for 72 h. After cooling to room temperature, the resulting solids were collected by filtration and washed several times with DMF and THF. The products were then further purified by Soxhlet extraction with DMF for three days. The isolated products were as follows: TPE-OPDI CMP as a dark brown solid (yield: 36 %), TPE-OPDI-Fe CMP as an amber-colored solid (yield: 36 %), TPE-OPDI-Co CMP as a brown solid (yield: 40 %), and TPE-OPDI-Ni CMP as a carrot-colored solid (yield: 58 %) [Fig. 1(a) and (b)].

3. Results and discussion

3.1. Synthesis and structural characterization of OPDI-2Br and OPDI-M-2Br monomers

We synthesized four monomers, OPDI-2Br, OPDI-Fe-2Br, OPDI-Co-2Br, and OPDI-Ni-2Br, and confirmed their chemical structures using

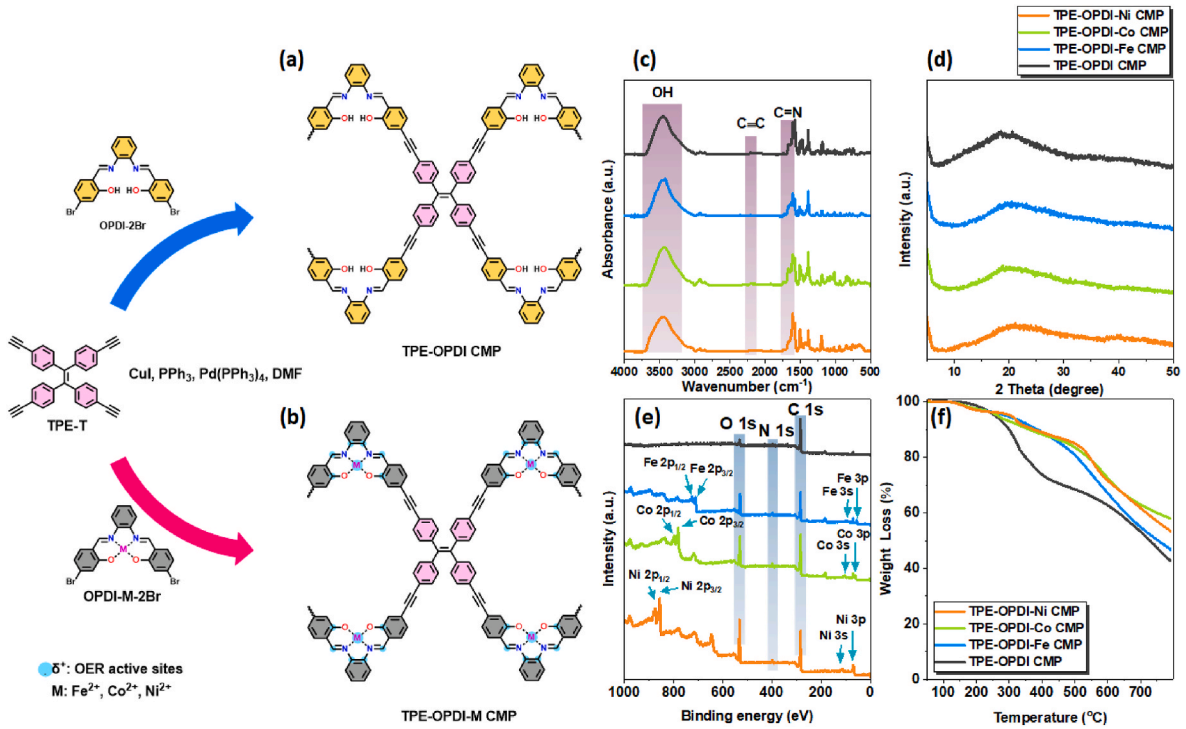

Fig. 1. Synthesis of (a) TPE-OPDI CMP and (b) TPE-OPDI-M CMPs by the Sonogashira coupling reaction and the corresponding (c) FTIR spectra, (d) XRD spectra, (e) XPS spectra, and (f) TGA profiles of TPE-OPDI CMP and TPE-OPDI-M CMPs.

FTIR and NMR analyses, as shown in Fig. S1–S5. For the OPDI-2Br series, which shares similar structural features, the FTIR spectrum revealed absorption bands centered around 1604 to 1616 cm^{-1}, corresponding to the C═N stretching vibrations formed during the Schiff base reaction. Additionally, distinct O–H stiretching bands were observed at approximately 3500 and 3200 cm^{-1}, as illustrated in Fig. S1. Fig. S2(a) unveiled the ^{1}H NMR spectrum of OPDI-2Br, displaying proton signals at 13.25, 8.94, 7.62, 7.47, 7.42, 7.19, and 7.17 ppm, which can be attributed to hydroxyl groups, imine units, and aromatic protons. The impact of metal coordination on the ^{1}H NMR spectra of OPDI-2Br derivatives is summarized in Fig. S3–S5. As shown in Fig. S3(a), the spectrum of OPDI-Fe-2Br exhibited no observable proton resonances. This complete signal quenching is ascribed to extreme paramagnetic broadening induced by high-spin Fe^{2+} centers (d^6 configuration, four unpaired electrons; Scheme S3). By contrast, the lower paramagnetism of high-spin Co^{2+} (d^7, three unpaired electrons; Scheme S4) and high-spin Ni^{2+} (d^8, two unpaired electrons [Scheme S5] allows for well-resolved spectra. OPDI-Co-2Br displays sharp resonances at 9.03, 8.88, 8.40, 8.28, 7.63, 7.53, 7.47, 7.38, and 7.18 ppm [Fig. S4(a)], which are assignable to imine (C═N), hydroxyl (O–H), and aromatic protons. Likewise, OPDI-Ni-2Br exhibits signals at 10.93, 8.11, 7.55, 7.54, 7.43, 7.42, and 7.07 ppm [Fig. S5(a)]. The preservation of narrow line widths in the Co^{2+} and Ni^{2+} complexes, compared to the fully broadened Fe^{2+} system, directly correlates with an unpaired electron count of each metal and resulting paramagnetism. These findings conclusively demonstrate that metal incorporation modulates the local electronic environment of the OPDI scaffold, with the degree of NMR signal suppression serving as a probe of the metal center's spin state. Complementary insights were provided by unveiling the ^{13}C NMR spectrum in Fig. S2(b). Imine and aromatic carbon signals of OPDI-2Br are disposed at 162, 161, 141, 133, 128, 126, 123, 122, 119, and 118 ppm. With metal incorporation, the ^{13}C NMR spectra of the metal-coordinated monomers also exhibited significant shifts. Specifically, OPDI-Fe-2Br showed no signals due to paramagnetic properties [Fig. S3(b)]; OPDI-Co-2Br displayed signals at 168, 158, 144, 137, 129, 128, 124, 119, 117, and 116 ppm [Fig. S4(b)]; and OPDI-Ni-2Br exhibited signals at 166, 157, 140, 135, 130, 128, 120, 118, and 117 ppm [Fig. S5(b)]. Overall, the combined ^{1}H NMR and ^{13}C NMR data confirm that metal incorporation into the OPDI-2Br structure leads to changes in the electronic environment and hybridization of the monomers, which is indicative of successful coordination between the OPDI structure and the metal species.

3.2. Synthesis and structural characterization of TPE-OPDI and TPE-OPDI-M CMPs

As depicted in Fig. 1(a)–1(b), TPE-T underwent Sonogashira coupling reactions with OPDI-2Br and its metal-coordinated derivatives, OPDI-Fe-2Br, OPDI-Co-2Br, and OPDI-Ni-2Br, yielding four CMPs, namely TPE-OPDI, TPE-OPDI-Fe, TPE-OPDI-Co, and TPE-OPDI-Ni CMPs. These materials, collectively referred to as TPE-based CMPs, were thoroughly characterized using FTIR, solid-state ^{13}C NMR, XRD, XPS, TGA, and spectroscopy to validate their structures. The FTIR spectra, presented in Fig. 1(c), revealed key characteristic peaks common to all TPE-based CMPs. A broad absorption in the range of 3083–3693 cm^{-1} was attributed to the O–H stretching vibrations from phenolic groups in the OPDI units, as shown in Scheme S2. A distinct peak near 2200 cm^{-1} indicated the presence of C≡C bonds, confirming the formation of alkynyl linkages between TPE and OPDI moieties [77–79]. Additionally, the absorption band observed around 1668 cm^{-1} corresponds to the C═N stretching vibration, indicating the formation of a Schiff base during the synthesis of OPDI-2Br and OPDI-*M*-2Br. The Raman spectra presented in Fig. S6 exhibit characteristic vibrational features observed across all TPE-OPDI CMP and TPE-OPDI-M CMP samples. Notably, a sharp peak at approximately 2205 cm^{-1} is assigned to the C≡C stretching vibration, confirming the presence of alkynyl linkages connecting the TPE and OPDI units, in agreement with the FTIR analysis.

Furthermore, a series of bands in the 1545-1650 cm^{-1} range can be attributed to the C═C stretching vibrations of aromatic rings, as well as C═N stretching associated with the imine groups, reflecting the integrity of the conjugated frameworks in both TPE-OPDI CMP and TPE-OPDI-M CMP materials. The solid-state ^{13}C NMR spectra further

supported the structural features of these CMPs. Carbon signals in the 100–200 ppm region were mainly attributed to aromatic carbon atoms, while peaks in the 90–100 ppm region were assigned to acetylenic carbons. Specifically, TPE-OPDI CMP exhibited signals at 143 ppm (C═C of TPE), 153 ppm (aromatic C–OH), and 161 ppm (C═N), as shown in Fig. S7. TPE-OPDI-Fe CMP displayed peaks at 139 ppm (C═C of TPE), 156 ppm (aromatic C–OH), and 161 ppm (C═N), as illustrated in Fig. S8. TPE-OPDI-Co CMP showed shifts to 140 ppm (C═C of TPE), 157 ppm (aromatic C–OH), and 163 ppm (C═N), as demonstrated in Fig. S9. TPE-OPDI-Ni CMP featured peaks at 143 ppm (C═C of TPE), 156 ppm (aromatic C–OH), and 161 ppm (C═N), as depicted in Fig. S10. X-ray diffraction (XRD) analysis, shown in Fig. 1(d), revealed broad, diffuse peaks across all samples, indicating their amorphous nature [80, 81]. A detailed structural analysis of the TPE-based CMPs was performed by X-ray photoelectron spectroscopy (XPS) to elucidate the bonding environments of carbon, nitrogen, oxygen, and the metal centers [Fig. 1 (e)]. The high-resolution C 1s spectra [Fig. S11(a)] reveal three main components: one at 283.6–284.2 eV, corresponding to **C**–C, **C**═C, and **C**≡C bonds; a second at 284.9–285.5 eV, attributable to **C**–N and **C**═N species; and a third at 285.6–286.5 eV, corresponding to **C**–O bonds. The N 1s region [Fig. S11(b)] can be deconvoluted into two peaks: 398.6–400.3 eV, assigned to imine (C═**N**) and (C–**N**) functionalities; and 398.7–398.9 eV, arising from metal-nitrogen coordination (Fe–**N**, Co–**N**, or Ni–**N**) in the corresponding CMPs. Likewise, the O 1s spectra [Fig. S11 (c)] features two components at 531.2–532.6 eV (phenolic C–O) and 529.7–531.3 eV, which we assign to metal-oxygen bonds (Fe–**O**, Co–**O**, or Ni–**O**). In Fig. 2, the high-resolution M 2p XPS spectra (M: Fe, Co, Ni) confirm the presence of divalent metal centers in the CMPs. The non-coordinated TPE-OPDI CMP [Fig. 2(a)] shows no discernible M 2p peaks, whereas TPE-OPDI-Fe CMP [Fig. 2(b)] exhibits Fe $2p_{3/2}$ and Fe $2p_{1/2}$ peaks at 710.7 eV and 724.3 eV, respectively, along with their characteristic satellite features, consistent with Fe^{2+}. TPE-OPDI-Co CMP [Fig. 2(c)] displays Co $2p_{3/2}$ and Co $2p_{1/2}$ signals at 781.3 eV and 797.2 eV, respectively, confirming Co^{2+} incorporation. TPE-OPDI-Ni CMP [Fig. 2(d)] shows Ni $2p_{3/2}$ and Ni $2p_{1/2}$ peaks at 856.5 eV and 874.2 eV, respectively, together with their satellites, indicative of Ni^{2+}. These well-defined doublets and satellite structures unambiguously verify the +2-oxidation state of Fe, Co, and Ni within the corresponding CMP networks [82].

Thermal stability of the TPE-based CMPs was evaluated by thermogravimetric analysis (TGA) under a nitrogen atmosphere in Fig. 1(f). The temperatures at 10 % weight loss (T_{d10}) for TPE-OPDI, TPE-OPDI-Fe, TPE-OPDI-Co, and TPE-OPDI-Ni were 300 °C, 387 °C, 363 °C, and 379 °C, respectively, as summarized in Fig. S12. Their corresponding char yields at 800 °C were 42.8, 46.8, 58.0, and 53.5 wt%. These data demonstrate that coordinating Fe, Co, or Ni to the conjugated structure significantly enhances both T_{d10} and the residual carbonaceous content. In particular, TPE-OPDI-Fe CMP exhibits the highest T_{d10} (387 °C), whereas TPE-OPDI-Co CMP affords the greatest char yield (58.0 wt%). This improvement in thermal robustness upon metal coordination underscores the stabilizing effect of Fe, Co, and Ni within the CMP network. Scanning electron microscopy (SEM) was used to elucidate the hierarchical, porous morphology of the TPE-OPDI CMP and TPE-OPDI-M CMP [Fig. 3]. In Fig. 3(a), TPE-OPDI appears as loosely packed, micron-scale aggregates with highly irregular, rough surfaces and pronounced interparticle voids, indicative of a three-dimensional porous network. Upon incorporating iron, the TPE-OPDI-Fe CMP resolves into densely interconnected nanoscale clusters with a characteristic sphere aggregate-like morphology, reflecting a dramatic increase in external surface area [Fig. 3(b)]. Cobalt coordination yields a similar nanocluster architecture in TPE-OPDI-Co CMP [Fig. 3(c)], but here plate-like subunits interweave among the clusters, producing a more pronounced mesoporous framework as evidenced by sharp edges and layered stacking. Finally, TPE-OPDI-Ni CMP exhibits larger aggregate networks punctuated by sponge-like channels and cavities on the order of hundreds of nanometers, confirming the presence of multiscale porosity throughout the polymer matrix [Fig. 3(d)]. Collectively, these SEM images demonstrate that all TPE-OPDI-M CMPs possess a robust, hierarchical pore structure, spanning micron-scale voids down to nanoscale clusters, which is ideally suited to facilitate rapid mass transport and maximize the exposure of catalytically active sites. Furthermore, transmission electron microscopy (TEM) analysis provided additional

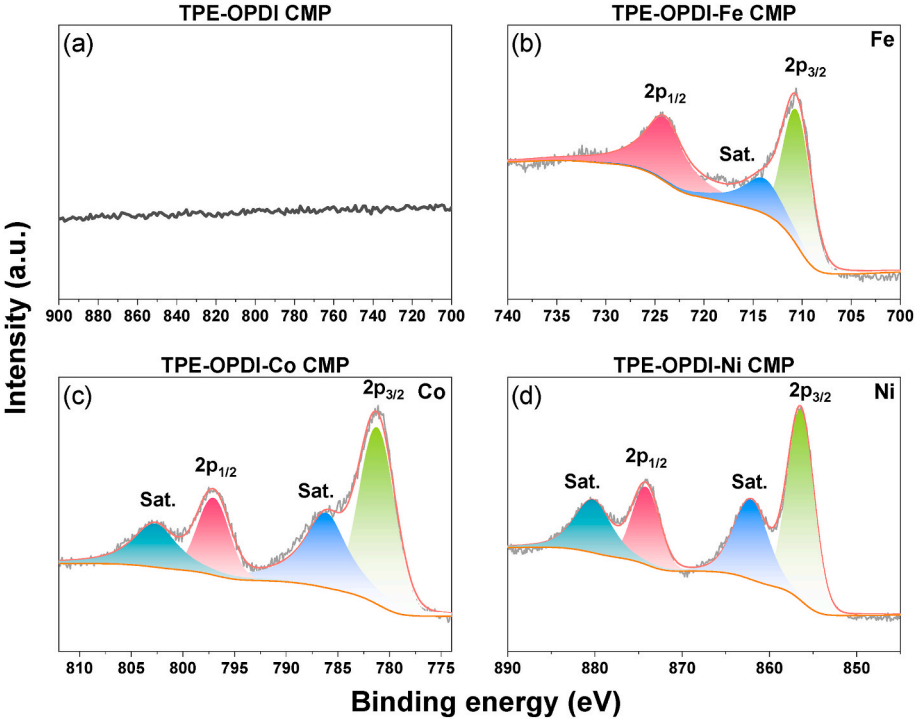

Fig. 2. (a) High-resolution XPS spectrum of TPE-OPDI CMP in the 700–900 eV range, Core-level XPS spectra of (b) TPE-OPDI-Fe CMP, (c) TPE-OPDI-Co CMP, and (d) TPE-OPDI-Ni CMP.

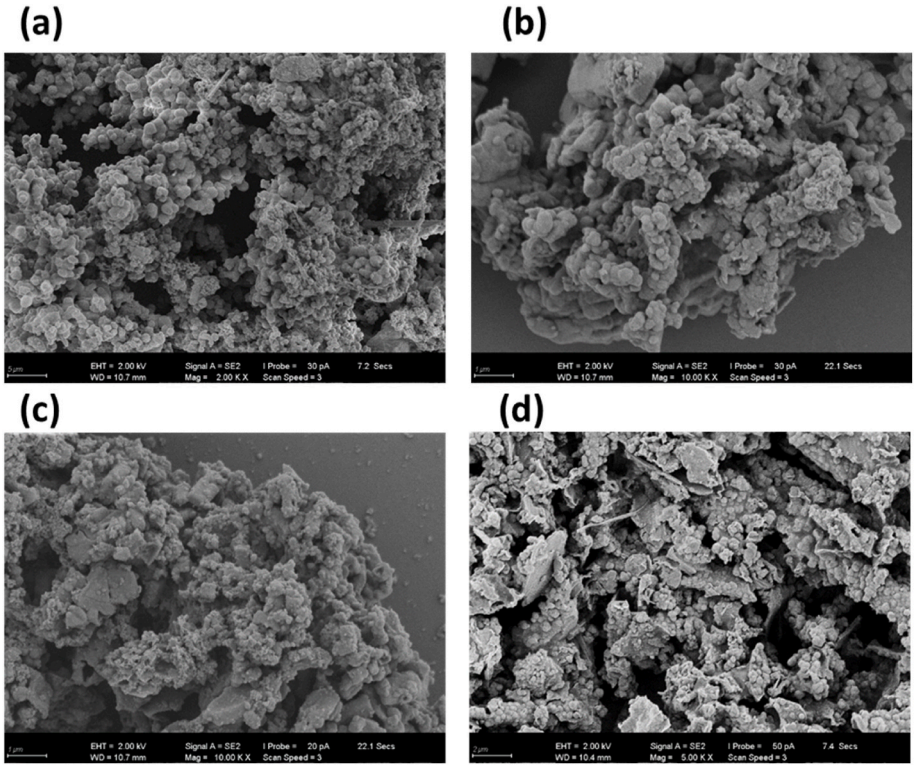

Fig. 3. SEM images of (a) TPE-OPDI, (b) TPE-OPDI-Fe, (c) TPE-OPDI-Co and (d) TPE-OPDI-Ni CMPs.

evidence for the hierarchical and porous architecture of the TPE-based CMPs, as shown in Fig. S13–S16. The TEM images of TPE-OPDI CMP [Fig. S13(a)–(c)] reveal loosely packed, micron-scale aggregates composed of irregular nanoparticles with rough surfaces and interparticle voids. This morphology suggests the formation of a lightly agglomerated network of nanoparticles that collectively construct the bulk polymer structure.

In the case of TPE-OPDI-Fe CMP [Fig. S14(a) and 14(b)], the TEM images display more compact, hierarchical clusters in which numerous nanoparticles have fused to form larger, rounded aggregates. By

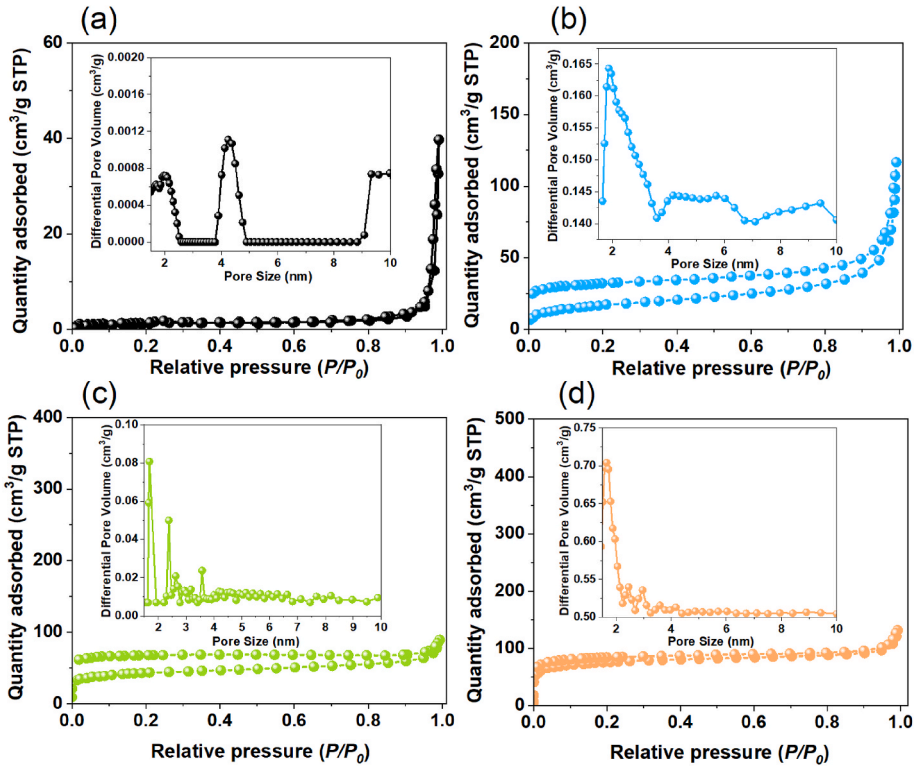

Fig. 4. N_2 adsorption/desorption isotherms and pore size distribution profiles of (a) TPE-OPDI, (b) TPE-OPDI-Fe, (c) TPE-OPDI-Co, and (d) TPE-OPDI-Ni CMPs.

contrast, TPE-OPDI-Co CMP [Fig. S15(a) and 15(b)] exhibits a distinctive nanocluster morphology, characterized by the presence of plate-like subunits and a pronounced mesoporous character, resulting in a layered and highly porous microstructure. TPE-OPDI-Ni CMP [Fig. S16(a) and 16(b)] shows more massive, blob-like polymer aggregates, which appear larger and denser than those observed for the Fe- or Co-based CMPs. Notably, the TPE-OPDI-Ni CMP structure features a network of bright regions and internal channels within the darker polymer matrix, indicating the presence of significant internal porosity. In addition, TEM-energy-dispersive X-ray spectroscopy (TEM-EDX) elemental mapping confirms the homogeneous distribution of carbon, nitrogen, oxygen, and the respective metal centers throughout the TPE-OPDI CMP and TPE-OPDI-M CMPs structures, further supporting the successful incorporation of metal ions into the polymer network [Fig. S13–S16]. The surface topology and porosity of the TPE-OPDI CMP and TPE-OPDI-M CMPs were investigated through nitrogen adsorption-desorption isotherm analysis. As depicted in Fig. 4(a)–4(d), TPE-OPDI CMP displayed a type III isotherm, characteristic of weak adsorbate-adsorbent interactions and indicative of predominantly macroporous or non-porous features. In contrast, TPE-OPDI-Fe CMP exhibited a type V isotherm similar to type IV behavior, suggestive of the presence of both microporous and mesoporous domains. Meanwhile, the isotherms of TPE-OPDI-Co and TPE-OPDI-Ni CMPs were classified as type IV with pronounced desorption hysteresis loops, reflecting typical mesoporous structures with capillary condensation effects. The Brunauer–Emmett–Teller (BET) analysis revealed that the specific surface areas of TPE-OPDI, TPE-OPDI-Fe, TPE-OPDI-Co, and TPE-OPDI-Ni CMPs were 4, 60, 154, and 281 $m^2\ g^{-1}$, respectively, demonstrating a substantial increase in surface area upon metal incorporation, particularly with Co and Ni coordination. Furthermore, pore size distribution was evaluated using non-local density functional theory (NLDFT), which confirmed the coexistence of micropores and mesopores across all samples. The dominant pore sizes were determined to be 2.01 nm for TPE-OPDI, 1.9 nm for TPE-OPDI-Fe, 1.6 nm for TPE-OPDI-Co, and 1.7 nm for TPE-OPDI-Ni, thereby corroborating the structural diversity introduced by different metal centers. These results stipulate that the particularly low surface area of the parent TPE-OPDI CMP network arises from its relatively planar, densely cross-linked architecture formed during the Sonogashira coupling of TPE-T and OPDI-2Br, which limits pore generation. In contrast, coordination of metal ions to the OPDI units introduces torsional strain into the backbone. When the distorted OPDI-*M*-2Br motifs undergo Sonogashira coupling with TPE-T to form the TPE-OPDI-M CMP networks, the resulting structures adopt a nonplanar configuration due to the torsional strain introduced by metal coordination.

This deviation from planarity disrupts the dense packing typically observed in the metal-free analogues and promotes the formation of a more open, porous architecture. Consequently, the metal-containing CMPs exhibit significantly increased surface areas and altered pore-size distributions relative to the pristine TPE-OPDI CMP network. This observation highlights a clear structure-property relationship, demonstrating that metal coordination serves as an effective strategy to modulate the porosity and enhance the catalytic accessibility of conjugated microporous polymers.

3.3. Electrocatalytic performance of TPE-OPDI and TPE-OPDI-M CMPs for oxygen evolution reaction

The intrinsic electrocatalytic activity towards the oxygen evolution reaction (OER) is achieved using a conventional three-electrode setup in 1 M KOH electrolyte. To fabricate a working electrode, the slurry of each sample was first prepared (details in the Supporting Information) and then drop-cast onto a Glassy Carbon Electrode (GCE). We initially conducted Linear Sweep Voltammetry (LSV) on both TPE-OPDI and TPE-OPDI-M CMPs (M = Fe^{2+}, Co^{2+}, and Ni^{2+}). As seen in Fig. 5(a), even with large overpotentials, TPE-OPDI CMP was unable to reach a current density of 10 mA cm^{-2}. But a noticeable reduction in overpotential to reach 10 mA cm^{-2} (η_{10}) was observed in the metal-coordinated CMPs [Fig. 5(b)]. TPE-OPDI-Co CMP required the lowest overpotential (η_{10}) of 400 mV, followed by TPE-OPDI-Fe CMP (467 mV) and TPE-OPDI-Ni CMP (502 mV), indicating that adding a transition metal into POPs can improve the catalytic OER activity [83]. In addition, TPE-OPDI-Co CMP has possessed an overpotential of only 80 and 40 mV higher than state-of-the-art catalysts like RuO_2 (~320 mV) [84,85] and IrO_2/C (~360 mV) [84], respectively. For further validation, the OER activity of each CMP was evaluated using the catalyst ink prepared without using carbon black. As shown in Fig. S17, the TPE-OPDI-Co CMP still exhibited higher OER catalytic activity. Consistently, the trend in OER catalytic activity was observed as TPE-OPDI-Co CMP > TPE-OPDI-Fe CMP > TPE-OPDI-Ni CMP > TPE-OPDI CMP. Moreover, the value of overpotential (η_{10}) for TPE-OPDI-Co CMP is lower or comparable with previously reported metal-coordinated POPs-based electrocatalysts, including COFs, CMPs, and MOFs (Table S1). To gain more understanding about OER kinetics, Tafel slopes of each electrocatalyst were calculated from LSV plots [Fig. 5(c)]. The lowest Tafel slope of TPE-OPDI-Co CMP (74 mV dec^{-1}) indicates better driving OER catalytic performance than TPE-OPDI-Fe CMP (117 mV dec^{-1}), TPE-OPDI-Ni CMP (183 mV dec^{-1}), and TPE-OPDI CMP (435 mV dec^{-1}). Remarkably, the Tafel slope of TPE-OPDI-Co CMP is lower than that of the state-of-the-art catalyst RuO_2 (115 mV dec^{-1}) [**84**]. Further, Cyclic voltammetry (CV) of each electrocatalyst was measured in the non-faradaic region as shown in Figures S18(a-d). From that, the slope of the $\Delta\ i/2$ versus scan rate graphs was used to compute the double-layer capacitance (C_{dl}) [Fig. 5(d)]. The calculated C_{dl} values of TPE-OPDI-Co CMP, TPE-OPDI-Fe CMP, TPE-OPDI-Ni CMP, and TPE-OPDI-CMP were 0.179, 0.055, 0.015, and 0.013 mF, respectively.

To get deep knowledge about the accessibility of active sites at the electrode surface for OER intermediates, the electrochemical active surface area (ECSA) has been measured for each electrocatalyst. The detailed derivation of ECSA has been discussed in the Supporting Information. As shown in Fig. S19, the TPE-OPDI-Co CMP demonstrated a high ECSA value of 4.47 cm^2. Whereas TPE-OPDI-Fe CMP, TPE-OPDI-Ni CMP, and TPE-OPDI CMP exhibited ECSA values of 1.37, 0.37, and 0.32 cm^2, respectively. These findings proved that TPE-OPDI-Co CMP possessed a superior OER activity among all prepared CMPs. Further, turnover frequency (TOF) was calculated for the TPE-OPDI-Co CMP at different overpotentials to evaluate the intrinsic electrocatalytic activity. The calculated TOF values for TPE-OPDI-Co CMP were found to be 1.7, 3.5, 7.6, 16.7, and 36.7 s^{-1} at 370, 395, 420, 445, and 470 mV, respectively (Fig. S20). Moreover, the observed current was normalized by the amount of catalyst loading onto the GCE to determine the mass activity. As shown in Fig. S21, the TPE-OPDI-Co CMP exhibited mass activity of 160 mA gm^{-1} at an overpotential of 450 mV. In contrast, the mass activity of TPE-OPDI-Fe CMP and TPE-OPDI-Ni CMP shows only 25 and 17 mA gm^{-1} at the same overpotential, respectively. In addition, we performed the catalytic activity of the TPE-OPDI CMP and TPE-OPDI-M CMPs for HER in alkaline and acidic electrolytes. The LSV was carried out to inspect the HER catalytic performance. It displayed that the TPE-OPDI-Co CMP needed the lowest overpotential values of 606, and 467 mV to reach a current density of 10 mA cm^{-2} in alkaline and acidic electrolytes, respectively [Fig. S22(a) and S22(b)]. Furthermore, to understand charge transfer resistance (R_{ct}) at the interface of electrode-electrolyte, an electrochemical impedance spectroscopy (EIS) study was conducted of all the electrocatalysts under OER conditions. The Randle equivalent circuit model was used to fit Nyquist plots. From the Nyquist plots [Fig. 5(e) and S23], it is depicted that R_{ct} values of TPE-OPDI-Co CMP, TPE-OPDI-Fe CMP, TPE-OPDI-Ni CMP, and TPE-OPDI CMP are 79.4, 159, 364.3, and 15450 Ω, respectively. These findings underscore that TPE-OPDI-Co CMP has fast kinetics at the electrode-electrolyte interface. Further, to check the stability of TPE-OPDI-Co CMP, the LSV was taken before and after 1000 CV cycles [Fig. 5(f)]. TPE-OPDI-Co CMP exhibited only a 7 mV change in overpotential (at 10 mA cm^{-2}), which showed the superior electrochemical stability of the catalyst. Along with

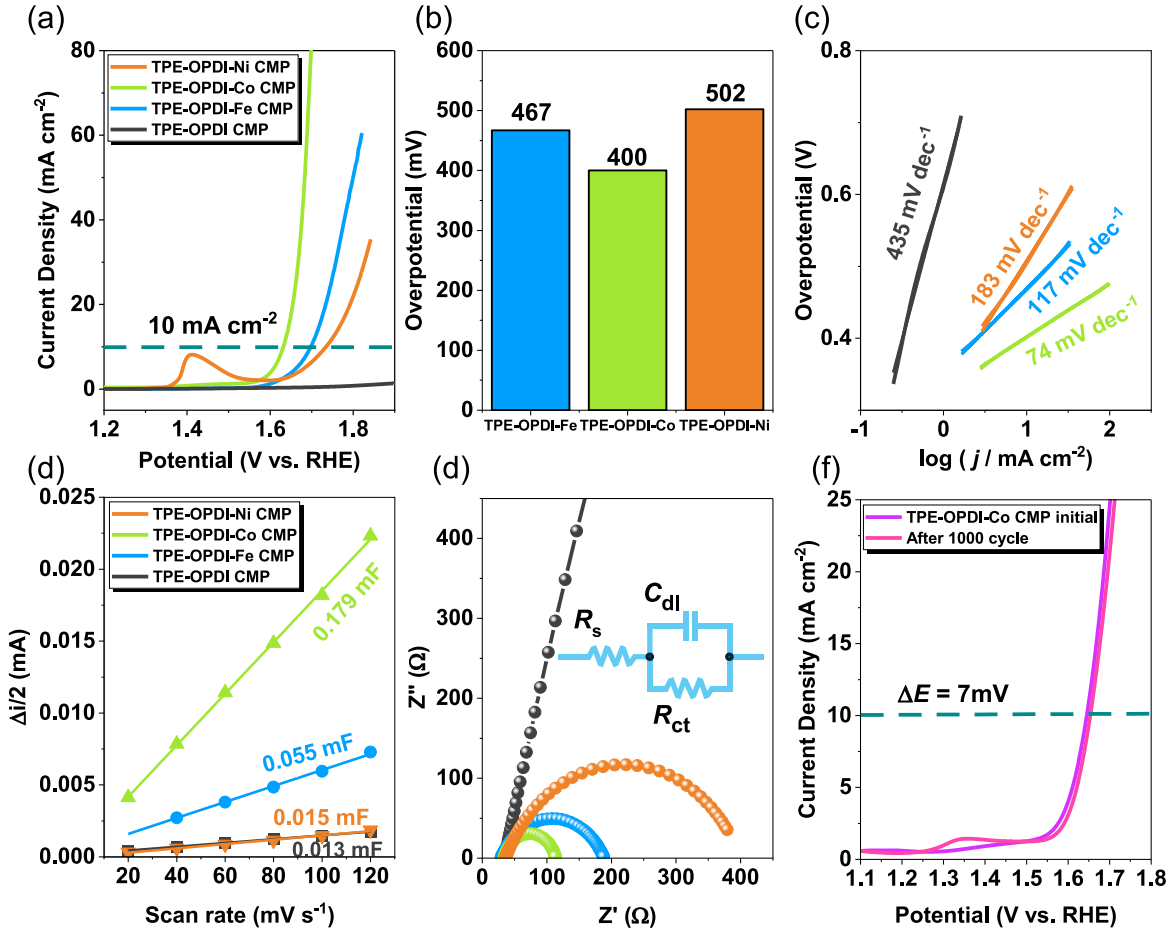

Fig. 5. Electrocatalytic OER performances of TPE-OPDI and TPE-OPDI-M based CMPs in 1 M KOH electrolyte. (a) OER polarization curve (LSV), (b) summarized values of overpotentials required to achieve 10 mA cm^{-2} current density, (c) Tafel plots, (d) Δ *i/2* versus scan rate plot for evaluating C_{dl}, (e) Nyquist plots of TPE-OPDI and TPE-OPDI-M based CMPs, and (f) LSV of TPE-OPDI-Co CMP before and after 1000 CV cycles.

the long-term stability of TPE-OPDI-CO CMP was further assessed using chronoamperometric (CA) measurements. As depicted in Fig. S24, the current density exhibited negligible decay after 15 h of continuous OER performance at three constant potentials (E_{app} = 1.60, 1.65, and 1.69 V vs. RHE) [Fig. S24(a)]. Furthermore, the retention of stable current density even after 50 h of CA testing highlights the excellent electrochemical steadiness of TPE-OPDI-Co CMP [Fig. S24(b)]. FTIR and SEM characterizations of TPE-OPDI-Co CMP were conducted before and after the stability test to evaluate potential chemical and morphological changes. The FTIR spectra show that the characteristic bands corresponding to aromatic C–H, alkyne C≡C, C═C, and C═N units remain intact after the stability test, indicating preservation of the chemical structure [Fig. S25]. SEM images further reveal that the overall porous architecture and surface morphology are largely retained following prolonged OER operation, demonstrating the material's structural integrity [Fig. S26]. As shown in Scheme S6, the OER in alkaline media follows the conventional adsorbate evolution mechanism (AEM), proceeding through sequential electron–proton transfers involving *OH, *O, and *OOH intermediates at the metal coordination sites (A-M, where M = Fe^{2+}, Co^{2+}, Ni^{2+}). These active sites originate from the well-defined salen-type chelation environment within the CMP framework, which ensures both electronic interaction and structural stability during catalysis. In addition to the M–OOH pathway, O_2 formation may also occur through M − O recombination. Among the three metals studied, TPE-OPDI-Co CMP exhibited the highest activity, which can be ascribed to two main factors: (i) the optimized electronic structure of Co^{2+} that provides favorable binding energies for OER intermediates, lowering the reaction barrier, and (ii) the efficient redox flexibility of Co^{2+}/Co^{3+}/Co^{4+}, enabling the generation of highly active Co–O species under alkaline conditions.

3.4. Density functional theory (DFT) study

Molecular electrostatic potential (MESP) analysis mapping serves as a valuable approach for visualizing the spatial distribution of electrostatic potential within a molecule, thereby offering insights into how molecular interactions may occur. As presented in Fig. S27, the MESP surfaces of TPE-OPDI CMP and its metal-coordinated analogues, TPE-OPDI-Fe, TPE-OPDI-Co, and TPE-OPDI-Ni CMPs, highlight significant regions of moderate electrostatic potential, shown in green. Regions of high electron density, visualized in red, are predominantly localized near oxygen atoms in all investigated structures, indicating potential electron-donating sites. In the case of pristine TPE-OPDI CMP, electron-deficient zones (depicted in blue) are limited to the hydroxyl-substituted segments attached to the peripheral aromatic units. In contrast, for the TPE-OPDI-M CMPs, electron-deficient areas are concentrated around the transition metal centers. These electrophilic regions are well-suited to interact with nucleophilic species, enhancing the adsorption of reaction intermediates involved in the OER, as seen in Fig. S27. Among TPE-OPDI-M CMPs, the regions surrounding the Fe and Ni are moderately nucleophilic, which hinders the interaction of incoming nucleophiles or the electron-rich species (*O, *OH, and *OOH), thus affecting the OER performance in comparison to the TPE-OPDI-Co CMP. This is because of the fact that TPE-OPDI-Co CMP has balanced potential (as shown in

Fig. S27) across the surface, offering a favorable environment to the incoming species.

The electronic characteristics of materials, especially the highest occupied molecular orbital (HOMO) and the lowest unoccupied molecular orbital (LUMO) are deeply influenced by their atomic arrangements and molecular frameworks. HOMO orbitals are primarily concerned with the capacity to deliver electrons, whereas LUMO orbitals are concerned solely with the affinity to accept electrons. Fig. 6 depicts the HOMO–LUMO distributions and corresponding energy levels for TPE-OPDI, TPE-OPDI-Fe, TPE-OPDI-Co, and TPE-OPDI-Ni CMPs. In the undoped TPE-OPDI CMP, the HOMO is extensively delocalized, spanning the molecular core and extending to the side arms, including heteroatomic regions. A comparable localization is evident in the metal-containing derivatives, with the HOMO concentrated in electron-rich domains, aligning well with findings from MESP analysis. This central electron density suggests improved donor characteristics, which can be advantageous in photocatalytic systems. On the other hand, LUMO distributions in TPE-OPDI-Fe, TPE-OPDI-Co, and TPE-OPDI-Ni CMPs deviate from that of pristine TPE-OPDI CMP. In the TPE-OPDI-M CMPs, the LUMOs are primarily localized around the transition metal sites, forming electron-deficient centers. These regions are likely to serve as binding sites for nucleophiles or adsorbed intermediates, enhancing molecular interactions during catalytic processes. The position of computed HOMO-LUMO suggests the overall behavior of investigated complexes towards the OER pathway as follows:

TPE-OPDI-Co CMP > TPE-OPDI-Fe CMP > TPE-OPDI-Ni CMP > TPE-OPDI CMP

3.5. The OER performance of TPE-OPDI-Co CMP

The activity of TPE-OPDI-Co CMP towards OER was assessed based on the value of $\eta_{OER.}$ The high values of η_{OER} correspond to the lower activity and vice versa. Thus, for the lower value of $\eta_{OER,}$ usually less amount of energy is required, and keeping this thing, the η_{OER} value was evaluated by considering the OER mechanism in the alkaline conditions. According to the OER mechanism, the geometries of three OER intermediates (*OH, *O, and *OOH) were optimized by placing them onto the surface of the TPE-OPDI-Co CMP. Based on these geometries, the Gibbs free energy of each PCET step for TPE-OPDI-Co was determined and displayed in Fig. S28 and Table S2. The first step, $* + OH^- \rightarrow *OH$, is moderately endergonic ($\Delta G_1 = 1.10$ eV), indicating feasible hydroxyl adsorption. This is necessary since OER is an endergonic process overall ($\Delta G_{OER} = 4.92$ eV), so to have ΔG_1 as endergonic is usually desired. The subsequent oxidation steps proceed through *O and *OOH intermediates, with the $*O \rightarrow *OOH$ step ($\Delta G_3 = 1.80$ eV) being the most energetically demanding and thus identified as the potential-determining step (PDS). Based on this value, the η_{OER} was calculated to be 0.57 V. It's generally considered that the DFT predicted OER catalysts with overpotentials in the range of 0.60 V [86] possess significant OER activities, which align well with the experimentally observed OER onset of 1.63 V maximum among all the synthesized CMPs. This agreement supports the Co^{2+} site as the active center and confirms the reliability of the computational model. The exergonic final step ($*OOH \rightarrow * + O_2$) further supports efficient O_2 desorption and catalyst regeneration.

4. Conclusions

We have demonstrated that pre-coordination of Fe^{2+}, Co^{2+}, and Ni^{2+} to OPDI-2Br monomers before Sonogashira coupling with TPE-T affords salen TPE-OPDI-Fe CMP, TPE-OPDI-Co CMP, and TPE-OPDI-Ni CMP networks as outstanding contenders for use as advanced electrocatalysts in high-efficiency OER with tunable backbone torsion, hierarchical porosity, and enhanced thermal robustness, based on TGA and BET measurements. Electrochemical measurements revealed that the TPE-OPDI-Co CMP exhibits the highest OER catalytic activity compared to TPE-OPDI-Fe CMP, TPE-OPDI-Ni CMP, and the pristine TPE-OPDI CMP. In particular, TPE-OPDI-Co CMP exhibits exceptional OER activity, which achieves 400 mV at 10 mA cm^{-2}, a 74 mV dec^{-1} Tafel slope, low charge-transfer resistance of 79.4 Ω, and excellent cycling stability, closely approaching the performance of precious-metal benchmarks. These findings establish a clear structure-property relationship whereby metal coordination introduces nonplanarity and free volume into CMPs, thereby maximizing accessible active sites and accelerating interfacial kinetics. This metal-templating approach offers a general platform for designing next-generation, earth-abundant electrocatalysts in water splitting and beyond.

CRediT authorship contribution statement

Yang-Chin Kao: Writing – review & editing, Writing – original draft, Investigation, Formal analysis, Data curation. **Tapomay Mondal:** Writing – review & editing, Formal analysis, Data curation. **Wei-Hsuan Chang:** Formal analysis, Data curation, Conceptualization. **Mohamed Gamal Mohamed:** Writing – review & editing, Writing – original draft,

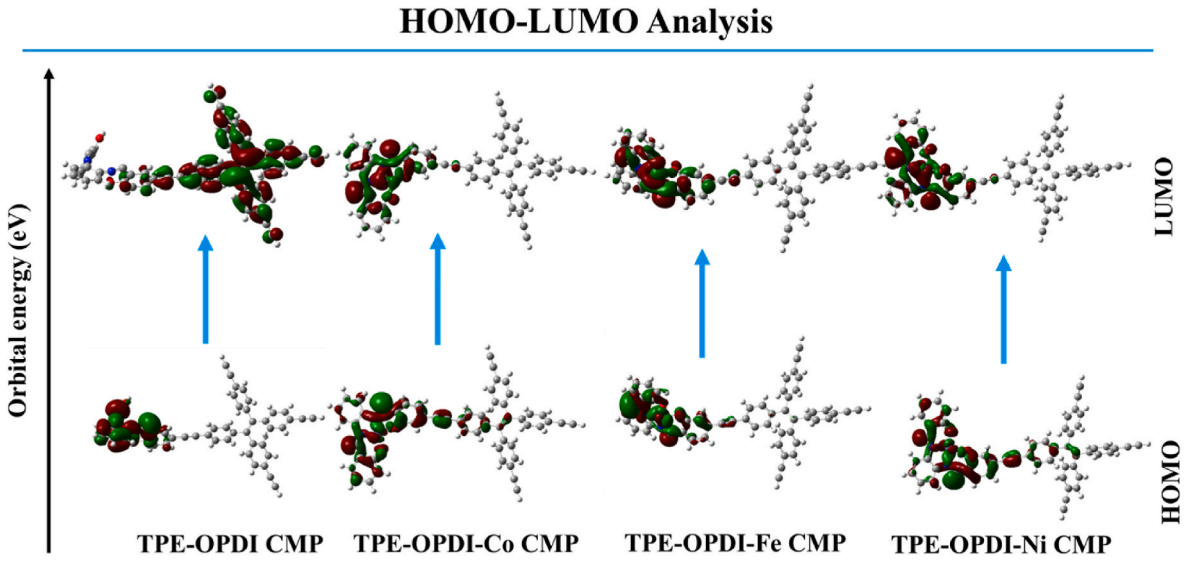

Fig. 6. The frontier molecular orbitals for the investigated TPE-OPDI CMP and TPE-OPDI-M CMPs at B3LYP/6–31 g(d,p).

Supervision, Methodology, Investigation, Formal analysis, Data curation, Conceptualization. **Shiao-Wei Kuo:** Supervision, Resources.

Data availability

Data will be made available on request.

Declaration of competing interest

The authors declare that they have no known competing financial interests or personal relationships that could have appeared to influence the work reported in this paper.

Acknowledgments

This study was supported financially by the National Science and Technology Council, Taiwan, under contracts NSTC 113-2223-E-110-001- and 113-2221-E-110-012-MY3. The authors thank the staff at National Sun Yat-sen University for their assistance with the TEM (ID: EM022600) experiments. The authors thank Hira Karim at National University of Sciences and Technology for her assistance with DFT simulation.

Appendix A. Supplementary data

Supplementary data to this article can be found online at https://doi.org/10.1016/j.ijhydene.2025.151390.

References

[1] Chu S, Majumdar A. Opportunities and challenges for a sustainable energy future. Nature 2012;488:294–303. https://doi.org/10.1038/nature11475.
[2] Mondal T, Mohamed MG, Mohamed AAK, Kuo SW. Construction of metal-coordinated bipyridine-based conjugated microporous polymers as robust electrocatalysts for hydrogen evolution. ACS Appl Energy Mater 2025;8:7703–13. https://doi.org/10.1021/acsaem.5c00992.
[3] Kabeyi MJB, Olanrewaju OA. Sustainable energy transition for renewable and low carbon grid electricity generation and supply. Front Energy Res 2022;9:743114. https://doi.org/10.3389/fenrg.2021.743114.
[4] Chatenet M, Pollet BG, Dekel DR, Dionigi F, Deseure J, Millet P, Braatz RD, Bazant MZ, Eikerling M, Staffell I, Balcombe P, Yang SH, Schäfer H. Water electrolysis: from textbook knowledge to the latest scientific strategies and industrial developments. Chem Soc Rev 2022;51:4583–762. https://doi.org/10.1039/D0CS01079K.
[5] Qian Q, Zhu Y, Ahmad N, Feng Y, Zhang H, Cheng M, Liu H, Xiao C, Zhang G, Xie Y. Recent advancements in electrochemical hydrogen production via hybrid water splitting. Adv Mater 2024;36:2306108. https://doi.org/10.1039/D0CS01079K.
[6] Deng R, Zhang B, Zhang Q. Electrochemical water splitting for scale hydrogen production: from the laboratory to industrial applications. ChemCatChem 2024;16:e202301165. https://doi.org/10.1002/cctc.202301165.
[7] Abdullah H, Shuwanto H, Lie J, Sillanpää M. Evaluation metrics and essential design strategies in developing electrode materials for a water-splitting process. Int J Hydrogen Energy 2024;64:695–723. https://doi.org/10.1016/j.ijhydene.2024.03.351.
[8] Zhang B, Shan J, Wang W, Tsiakaras P, Li Y. Oxygen vacancy and core–shell heterojunction engineering of anemone-like CoP@ CoOOH bifunctional electrocatalyst for efficient overall water splitting. Small 2022;18:2106012. https://doi.org/10.1002/smll.202106012.
[9] Yang N, Tian S, Feng Y, Hu Z, Liu H, Tian X, Xu L, Hu C, Yang J. Introducing high-valence iridium single atoms into bimetal phosphides toward high-efficiency oxygen evolution and overall water splitting. Small 2023;19:2207253. https://doi.org/10.1002/smll.202207253.
[10] Sari FNI, Abdillah S, Ting JM. FeOOH-containing hydrated layered iron vanadate electrocatalyst for superior oxygen evolution reaction and efficient water splitting. J Chem Eng 2021;416:129165. https://doi.org/10.1016/j.cej.2021.129165.
[11] Shuwanto H, Lie J, Abdullah H, Pasaribu SP, Masmur I, Tiffany, Nur NS. Kastario, seaweed-like structure of a $NiCo_2O_4$/$NiFe_2O_4$/C nanoelectrocatalyst: an effective strategy for boosting overall water splitting. ACS Appl Energy Mater 2025;8:4321–30. https://doi.org/10.1021/acsaem.4c03261.
[12] Song J, Wei C, Huang ZF, Liu C, Zeng L, Wang X, Xu ZJ. A review on fundamentals for designing oxygen evolution electrocatalysts. Chem Soc Rev 2020;49:2196–214. https://doi.org/10.1039/C9CS00607A.
[13] Zhu K, Shi F, Zhu X, Yang W. The roles of oxygen vacancies in electrocatalytic oxygen evolution reaction. Nano Energy 2020;73:104761. https://doi.org/10.1016/j.nanoen.2020.104761.
[14] Singh TI, Rajeshkhanna G, Pan UN, Kshetri T, Lin H, Kim NH, Lee JH. Alkaline water splitting enhancement by MOF-derived Fe–Co–oxide/Co@ NC-mNS heterostructure: boosting OER and HER through defect engineering and in situ oxidation. Small 2021;17:2101312. https://doi.org/10.1002/smll.202101312.
[15] Cao M, Lu D, Zhong DC, Lu TB. Prussian blue analogues and their derived nanomaterials for electrocatalytic water splitting. Coord Chem Rev 2020;407:213156. https://doi.org/10.1016/j.ccr.2019.213156.
[16] Sun S, Shen G, Jiang J, Mi W, Liu X, Pan L, Zhang X, Zou JJ. Boosting oxygen evolution kinetics by Mn–N–C motifs with tunable spin state for highly efficient solar-driven water splitting. Adv Energy Mater 2019;9:1901505. https://doi.org/10.1002/aenm.201901505.
[17] Chong L, Wen J, Song E, Yang Z, Bloom ID, Ding W. Synergistic Co-Ir/Ru composite electrocatalysts impart efficient and durable oxygen evolution catalysis in acid. Adv Energy Mater 2023;13:2302306. https://doi.org/10.1002/aenm.202302306.
[18] Choi MJ, Wang L, Stoerzinger KA, Chung SY, Chambers SA, Du Y. Epitaxial design of complex nickelates as electrocatalysts for the oxygen evolution reaction. Adv Energy Mater 2023;13:2300239. https://doi.org/10.1002/aenm.202300239.
[19] Jose V, Hu H, Edison E, Manalastas Jr W, Ren H, Kidkhunthod P, Sreejith S, Jayakumar A, Nsanzimana JMV, Srinivasan M, Choi J, Lee JM. Modulation of single atomic Co and Fe sites on hollow carbon nanospheres as oxygen electrodes for rechargeable Zn-air batteries. Small Methods 2021;5:2000751. https://doi.org/10.1002/smtd.202000751.
[20] Xie X, Du L, Yan L, Park S, Qiu Y, Sokolowski J, Wang W, Shao Y. Oxygen evolution reaction in alkaline environment: material challenges and solutions. Adv Funct Mater 2022;32:2110036. https://doi.org/10.1002/adfm.202110036.
[21] Srinivas K, Chen Y, Wang B, Yu B, Wang X, Hu Y, Lu Y, Li W, Zhang W, Yang D. Metal–organic framework-derived NiS/Fe_3O_4 heterostructure-decorated carbon nanotubes as highly efficient and durable electrocatalysts for oxygen evolution reaction. ACS Appl Mater Interfaces 2020;12:31552–63. https://doi.org/10.1021/acsami.0c09737.
[22] Pan Q, Wang L. Recent perspectives on the structure and oxygen evolution activity for non-noble metal-based catalysts. J Power Sources 2021;485:229335. https://doi.org/10.1016/j.jpowsour.2020.229335.
[23] Luo R, Qian Z, Xing L, Du C, Yin G, Zhao S, Du L. Re-Looking into the active moieties of metal X-ides (X-= phosph-, sulf-, nitr-, and carb-) toward oxygen evolution reaction. Adv Funct Mater 2021;31:2102918. https://doi.org/10.1002/adfm.202102918.
[24] Liu H, Guan J, Yang S, Yu Y, Shao R, Zhang Z, Dou M, Wang F, Xu Q. Metal–organic-framework-derived Co_2P nanoparticle/multi-doped porous carbon as a trifunctional electrocatalyst. Adv Mater 2020;32:2003649. https://doi.org/10.1002/adma.202003649.
[25] Wang Z, Zhou Q, Zhu Y, Du Y, Yang W, Chen Y, Wang S. NiFeMn-layered double hydroxides linked by graphene as high-performance electrocatalysts for oxygen evolution reaction. Nanomaterials 2022;12:2200. https://doi.org/10.3390/nano12132200.
[26] Ni S, Qu H, Xing H, Xu Z, Zhu X, Yuan M, Wang L, Yu J, Li Y, Yang L, Liu H. Donor–acceptor couples of metal and metal oxides with enriched Ni^{3+} active sites for oxygen evolution. ACS Appl Mater Interfaces 2021;13:17501–10. https://doi.org/10.1021/acsami.1c00890.
[27] Qian Q, Li Y, Liu Y, Zhang G. General anion-exchange reaction derived amorphous mixed-metal oxides hollow nanoprisms for highly efficient water oxidation electrocatalysis. Appl Catal B Environ 2020;266:118642. https://doi.org/10.1016/j.apcatb.2020.118642.
[28] Li L, Wang P, Shao Q, Huang X. Recent progress in advanced electrocatalyst design for acidic oxygen evolution reaction. Adv Mater 2021;33:2004243. https://doi.org/10.1002/adma.202004243.
[29] Liu T, Chen C, Pu Z, Huang Q, Zhang X, Al-Enizi AM, Nafady A, Huang S, Chen D, Mu S. Non-Noble-metal-based electrocatalysts for acidic oxygen evolution reaction: recent progress, challenges, and perspectives. Small 2024;20:2405399. https://doi.org/10.1002/smll.202405399.
[30] Han H, Kim I, Park S. Thermally templated cobalt oxide nanobubbles on crumpled graphene sheets: a promising non-precious metal catalysts for acidic oxygen evolution. Electrochim Acta 2021;382:138277. https://doi.org/10.1016/j.electacta.2021.138277.
[31] Mohamed MG, Chen CC, Ibrahim M, Mousa AO, Elsayed MH, Ye Y, Kuo SW. Tetraphenylanthraquinone and dihydroxybenzene-tethered conjugated microporous polymer for enhanced CO_2 uptake and supercapacitive energy storage. JACS Au 2024;4:3593–605. https://doi.org/10.1021/jacsau.4c0053.7.
[32] Samy MM, Mohamed MG, Sharma SU, Chaganti SV, Lee JT, Kuo SW. An Ultrastable Tetrabenzonaphthalene-Linked conjugated microporous polymer functioning as a high-performance electrode for supercapacitors. J Taiwan Inst Chem Eng 2024;158:104750. https://doi.org/10.1016/j.jtice.2023.104750.
[33] Basit A, Kao YC, El-Ossaily YA, Kuo SW, Mohamed MG. Rational engineering and synthesis of pyrene and thiazolo[5,4-d] thiazole-functionalized conjugated microporous polymers for efficient supercapacitor energy storage. J Mater Chem A 2024;12:30508–21. https://doi.org/10.1039/D4TA05908E.
[34] Mohamed MG, El-Mahdy AFM, Kotp MG, Kuo SW. Advances in porous organic polymers: syntheses, structures, and diverse applications. Mater Adv 2022;3:707–33. https://doi.org/10.1039/D1MA00771H.
[35] Samy MM, Mekhemer IMA, Mohamed MG, Elsayed MH, Lin KH, Chen YK, Wu TL, Chou HH, Kuo SW. Conjugated microporous polymers incorporating Thiazolo [5,4-d] thiazole moieties for Sunlight-Driven hydrogen production from water. Chem Eng J 2022;446:137158. https://doi.org/10.1016/j.cej.2022.137158.
[36] Chang SY, Elewa AM, Mohamed MG, Mekhemer IMA, Samy MM, Zhang K, Chou HH, Kuo SW. Rational design and synthesis of bifunctional Dibenzo [g,p] chrysene-based conjugated microporous polymers for energy storage and visible light-driven photocatalytic hydrogen evolution. Mater Today Chem 2023;33:101680. https://doi.org/10.1016/j.mtchem.2023.101680.

[37] Mohamed MG, Sharma SU, Wang PT, Ibrahim M, Lin MH, Liu CL, Ejaz M, Yen HJ, Kuo SW. Construction of fully π-conjugated, diyne-linked conjugated microporous polymers based on tetraphenylethene and dibenzo [g, p] chrysene units for energy storage. Polym Chem 2024;15:2827–39. https://doi.org/10.1039/D4PY00421C.
[38] Lee J, Cooper AI. Advances in conjugated microporous polymers. Chem Rev 2020; 120:2171–214. https://doi.org/10.1021/acs.chemrev.9b00399.
[39] Sivasurya E, Atchudan R, Mohamed MG, Thangamani A, Rajendran S, Jalil A, Kalambate PK, Manoj D, Kuo SW. Electrocatalytic conversion of CO_2 into selective carbonaceous fuels using metal-organic frameworks: an overview of recent progress and perspectives. Mater Today Chem 2025;44:102538. https://doi.org/10.1016/j.mtchem.2025.102538.
[40] Chung WT, Mekhemer IMA, Mohamed MG, Elewa AM, El-Mahdy AFM, Chou HH, Kuo SW, Wu KCW. Recent advances in metal/covalent organic frameworks based materials: their synthesis, structure design and potential applications for hydrogen production. Coord Chem Rev 2023;483:215066. https://doi.org/10.1016/j.ccr.2023.215066.
[41] Kao YC, Yeh KT, Mohamed MG, Karim H, Su WH, Kuo SW. Structural modulation via mesoporous silica templating in covalent organic frameworks: converting functional aspects for adsorption behavior. Sep Purif Technol 2025;375:133827. https://doi.org/10.1016/j.seppur.2025.133827.
[42] Mekhemer IMA, Elewa AM, Elsenety MM, Samy MM, Mohamed MG, Musa AF, Huang TF, Wei TC, Kuo SW, Chen BH, Yang SD, Chou HH. Self-condensation for enhancing the hydrophilicity of covalent organic polymers and photocatalytic hydrogen generation with unprecedented apparent quantum yield up to 500 nm. Chem Eng J 2024;497:154280. https://doi.org/10.1016/j.cej.2024.154280.
[43] Mohamed MG, Elewa AM, Chen NP, Mohammed AAK, Kuo SW. Construction of malononitrile-functionalized conjugated microporous polymers as adsorbents for effective adsorption of Rhodamine B and density functional theory perspective. Colloids Surf A Physicochem Eng Asp 2025;721:137214. https://doi.org/10.1016/j.colsurfa.2025.137214.
[44] Mohamed MG, Atayde Jr EC, Matsagar BM, Na J, Yamauchi Y, Wu KCW, Kuo SW. Construction hierarchically mesoporous/microporous materials based on block copolymer and covalent organic framework. J Taiwan Inst Chem Eng 2020;112: 180–92. https://doi.org/10.1016/j.jtice.2020.06.013.
[45] Mohamed MG, Chang SY, Ejaz M, Samy MM, Mousa AO, Kuo SW. Design and synthesis of bisulfone-linked two-dimensional conjugated microporous polymers for CO_2 adsorption and energy storage. Molecules 2023;28:3234. https://doi.org/10.3390/molecules28073234.
[46] Ali SA, Sadiq I, Ahmad T. Superlative porous organic polymers for photochemical and electrochemical CO_2 reduction applications: from synthesis to functionality. Langmuir 2024;40:10414–32. https://doi.org/10.1021/acs.langmuir.4c00310.
[47] Cui X, Lei S, Wang AC, Gao L, Zhang Q, Yang Y, Lin Z. Emerging covalent organic frameworks tailored materials for electrocatalysis. Nano Energy 2020;70:104525. https://doi.org/10.1016/j.nanoen.2020.104525.
[48] Xiao L, Wang Z, Guan J. Optimization strategies of covalent organic frameworks and their derivatives for electrocatalytic applications. Adv Funct Mater 2024;34: 2310195. https://doi.org/10.1002/adfm.202310195.
[49] Yusran Y, Li H, Guan X, Fang Q, Qiu S. Covalent organic frameworks for catalysis. Energy Chem 2020;2:100035. https://doi.org/10.1016/j.enchem.2020.100035.
[50] Zhao Q, Zhang Q, Xu Y, Han A, He H, Zheng H, Zheng W, Lei H, Apfel UP, Cao R. Improving active site local proton transfer in porous organic polymers for boosted oxygen electrocatalysis. Angew Chem Int Ed 2024;63:e202414104. https://doi.org/10.1002/anie.202414104.
[51] Liao PQ, Shen JQ, Zhang JP. Metal-organic frameworks for electrocatalysis. Coord Chem Rev 2018;373:22–48. https://doi.org/10.1016/j.ccr.2017.09.001.
[52] Li D, Xu HQ, Jiao L, Jiang HL. Metal-organic frameworks for catalysis: state of the art, challenges, and opportunities. Energy Chem 2019;1:100005. https://doi.org/10.1016/j.enchem.2019.100005.
[53] Chen H, Liang X, Liu Y, Ai X, Asefa T, Zou X. Active site engineering in porous electrocatalysts. Adv Mater 2020;32:2002435. https://doi.org/10.1002/adma.202002435.
[54] Wang Q, Astruc D. State of the art and prospects in metal–organic framework (MOF)-based and MOF-derived nanocatalysis. Chem Rev 2019;120:1438–511. https://doi.org/10.1021/acs.chemrev.9b00223.
[55] Chen YZ, Zhang R, Jiao L, Jiang HL. Metal–organic framework-derived porous materials for catalysis. Coord Chem Rev 2018;362:1–23. https://doi.org/10.1016/j.ccr.2018.02.008.
[56] Kaur P, Hupp JT, Nguyen ST. Porous organic polymers in catalysis: opportunities and challenges. ACS Catal 2011;1:819–35. https://doi.org/10.1021/cs200131g.
[57] Rani R, Deep A, Mizaikoff B, Singh S. Enhanced hydrothermal stability of Cu MOF by post synthetic modification with amino acids. Vacuum 2019;164:449–57. https://doi.org/10.1016/j.vacuum.2019.01.011.
[58] Zhou YB, Zhan ZP. Conjugated microporous polymers for heterogeneous catalysis. Chem Asian J 2018;13:9–19. https://doi.org/10.1002/asia.201701107.
[59] Hu Z, Peng Y, Kang Z, Qian Y, Zhao D. A modulated hydrothermal (MHT) approach for the facile synthesis of UiO-66-type MOFs. Inorg Chem 2015;54:4862–8. https://doi.org/10.1021/acs.inorgchem.5b00435.
[60] Leus K, Bogaerts T, De Decker J, Depauw H, Hendrickx K, Vrielinck H, Speybroeck VV, Van Der Voort P. Systematic study of the chemical and hydrothermal stability of selected "stable" Metal Organic Frameworks. Microporous Mesoporous Mater 2016;226:110–6. https://doi.org/10.1016/j.micromeso.2015.11.055.
[61] Al-Janabi N, Deng H, Borges J, Liu X, Garforth A, Siperstein FR, Fan X. A facile post-synthetic modification method to improve hydrothermal stability and CO_2 selectivity of CuBTC metal–organic framework. Ind Eng Chem Res 2016;55: 7941–9. https://doi.org/10.1021/acs.iecr.5b04217.
[62] Hu Y, Liu J, Lee C, Li M, Han B, Wu T, Pan H, Genga D, Yan Q. Integration of metal–organic frameworks and metals: synergy for electrocatalysis. Small 2023;19: 2300916. https://doi.org/10.1002/smll.202300916.
[63] Xing G, Liu S, Sun GY, Liu JY. Modification of metals and ligands in two-dimensional conjugated metal-organic frameworks for CO_2 electroreduction: a combined density functional theory and machine learning study. J Colloid Interface Sci 2025;677:111–9. https://doi.org/10.1016/j.jcis.2024.08.069.
[64] Bavykina A, Kolobov N, Khan IS, Bau JA, Ramirez A, Gascon J. Metal–organic frameworks in heterogeneous catalysis: recent progress, new trends, and future perspectives. Chem Rev 2020;120:8468–535. https://doi.org/10.1021/acs.chemrev.9b00685.
[65] Chen L, Xu Q. Metal-organic framework composites for catalysis. Matter 2019;1: 57–89. https://doi.org/10.1016/j.matt.2019.05.018.
[66] Liu C, Li H, Liu F, Chen J, Yu Z, Yuan Z, Wang C, Zheng H, Henkelman G, Wei L, Chen Y. Intrinsic activity of metal centers in metal–nitrogen–carbon single-atom catalysts for hydrogen peroxide synthesis. J Am Chem Soc 2020;142:21861–71. https://doi.org/10.1021/jacs.0c10636.
[67] Freire C, Nunes M, Pereira C, Fernandes DM, Peixoto AF, Rocha M. Metallo (salen) complexes as versatile building blocks for the fabrication of molecular materials and devices with tuned properties. Coord Chem Rev 2019;394:104–34. https://doi.org/10.1016/j.ccr.2019.05.014.
[68] Quinones YN, Paniak TJ, Lee YE, Kim SM, Tcyrulnikov S, Kozlowski MC. Chromium-salen catalyzed cross-coupling of phenols: mechanism and origin of the selectivity. J Am Chem Soc 2019;141:10016–32. https://doi.org/10.1021/jacs.9b03890.
[69] Crane AK, MacLachlan MJ. Portraits of porosity: porous structures based on metal salen complexes, vol.2012. EurJIC; 2012. p. 17–30. https://doi.org/10.1002/ejic.201100786.
[70] Liu JH, Yang LM, Ganz E. Electrocatalytic reduction of CO_2 by two-dimensional transition metal porphyrin sheets. J Mater Chem A 2019;7:11944–52. https://doi.org/10.1039/C9TA01188A.
[71] Hayat A, Sohail M, El Jery A, Al-Zaydi KM, Raza S, Ali H, Al-Hadeethi Y, Taha TA, Din IU, Khan MA, Amin MA, Ghasali E, Orooji Y, Ajmal Z, Ansari MZ. Recent advances in ground-breaking conjugated microporous polymers-based materials, their synthesis, modification and potential applications. Mater Today 2023;64: 180–208. https://doi.org/10.1016/j.mattod.2023.02.025.
[72] Shi Z, Yang W, Gu Y, Liao T, Sun Z. Metal-nitrogen-doped carbon materials as highly efficient catalysts: progress and rational design. Adv Sci 2020;7:2001069. https://doi.org/10.1002/advs.202001069.
[73] Mohamed MG, Chen TC, Kuo SW. Solid-state chemical transformations to enhance gas capture in benzoxazine-linked conjugated microporous polymers. Macromolecules 2021;54:5866–77. https://doi.org/10.1021/acs.macromol.1c00736.
[74] Mohamed MG, Chang WC, Kuo SW. Crown ether-and benzoxazine-linked porous organic polymers displaying enhanced metal ion and CO_2 capture through solid-state chemical transformation. Macromolecules 2022;55:7879–92. https://doi.org/10.1021/acs.macromol.2c01216.
[75] Weng TH, Mohamed MG, Sharma SU, Mekhemer IMA, Chou HH, Kuo SW. Rationally engineered Ultrastable three-dimensional (3D) conjugated microporous polymers containing Triptycene, tetraphenylethene, and benzothiadiazole units as exceptional high-performance organic electrodes for supercapacitors. ACS Appl Energy Mater 2023;6:9012–24. https://doi.org/10.1021/acsaem.3c01933.
[76] Weng TH, Mohamed MG, Sharma SU, Chaganti SV, Samy MM, Lee JT, Kuo SW. Ultrastable three-dimensional triptycene- and tetraphenylethene-conjugated microporous polymers for energy storage. ACS Appl Energy Mater 2022;5: 14239–49. https://doi.org/10.1021/acsaem.2c02809.
[77] Singh PN, Mohamed MG, Kotp MG, Mondal T, Chaganti SV, Ibrahim M, Sharma SU, Ye Y, Kuo SW. Nitrogen- and sulfur-rich microporous carbons derived from Conjug3764ated microporous polymers for CO_2 uptake, supercapacitor energy storage, and electrochemical hydrogen production. ACS Appl Polym Mater 2025;7:3324–36. https://doi.org/10.1021/acsapm.5c00012.
[78] Mohamed MG, Basit A, Shih CY, Sharma SU, Mondal T, Kuo SW. Pyrene-linked covalent organic polymer/single-walled carbon nanotubes hybrids as high-performance electrodes for supercapacitive energy storage. ACS Appl Energy Mater 2025;8:3764–78. https://doi.org/10.1021/acsaem.5c00052.
[79] Mohamed MG, Su BX, Kuo SW. Robust nitrogen-doped microporous carbon via crown ether-functionalized benzoxazine-linked porous organic polymers for enhanced CO_2 adsorption and supercapacitor applications. ACS Appl Mater Interfaces 2024;16:40858–72. https://doi.org/10.1021/acsami.4c05645.
[80] Huang SY, Lin X, Yang HY, Dou XR, Shi WJ, Deng JH, Zhong DC, Gong YN, Lu TB. Covalent bonding of salen metal complexes with pyrene chromophores to porous polymers for photocatalytic hydrogen evolution. Inorg Chem 2024;63:13594–601. https://doi.org/10.1021/acs.inorgchem.4c01774.
[81] Wu W, Dong Z, Chen M, Li W, Liao A, Liu Q, Zhang Y, Zhou Z, Zeng C, Gong X, Dai C. Metal–Salen-Incorporated conjugated microporous polymers as robust artificial leaves for solar-driven reduction of atmospheric CO_2 with H_2O. Carbon Energy 2025;7:e646doi. https://doi.org/10.1002/cey2.646.
[82] Zhang B, Chen L, Zhang Z, Li Q, Khangale P, Hildebrandt D, Liu X, Feng Q, Qiao S. Modulating the band structure of metal coordinated salen COFs and an in situ constructed charge transfer heterostructure for electrocatalysis hydrogen evolution. Adv Sci 2022;9:2105912. https://doi.org/10.1002/advs.202105912.
[83] Zhou W, Yang L, Zhou FY, Deng QW, Wang X, Zhai D, Ren GQ, Han KL, Deng WQ, Sun L. Salen-based conjugated microporous polymers for efficient oxygen evolution reaction. Chem Eur J 2020;26:7720–6. https://doi.org/10.1002/chem.202001039.

[84] Z, Liu Y, Ma W, Gu C, Yuan F. Teng, Facile synthesis of MoxC-FeNi@NC with an OER activity superior to RuO_2 and IrO_2/C. J Phys Chem Solids 2020;147:109578. https://doi.org/10.1016/j.jpcs.2020.109578.

[85] Qin Y, Yu T, Deng S, Zhou XY, Lin D, Zhang Q, Jin Z, Zhang D, He YB, Qiu HJ, He L, Kang F, Li K, Zhang TY. RuO_2 electronic structure and lattice strain dual engineering for enhanced acidic oxygen evolution reaction performance. Nat Commun 2022;13:3784. https://doi.org/10.1038/s41467-022-31468-0.

[86] Ha M, Kim DY, Umer M, Gladkikh V, Myung CW, Kim KS. Tuning metal single atoms embedded in N_xC_y moieties toward high-performance electrocatalysis. Energy Environ Sci 2021;14:3455–68. https://doi.org/10.1039/D1EE00154J.